Faraday Discussions

Accepted Manuscript

This manuscript will be presented and discussed at a forthcoming Faraday Discussion meeting. All delegates can contribute to the discussion which will be included in the final volume.

Register now to attend! Full details of all upcoming meetings: http://rsc.li/fd-upcoming-meetings

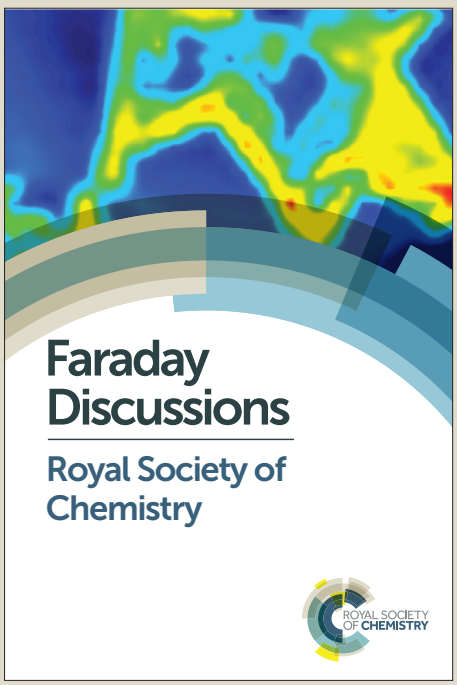

This is an *Accepted Manuscript*, which has been through the Royal Society of Chemistry peer review process and has been accepted for publication.

Accepted Manuscripts are published online shortly after acceptance, before technical editing, formatting and proof reading. Using this free service, authors can make their results available to the community, in citable form, before we publish the edited article. We will replace this *Accepted Manuscript* with the edited and formatted *Advance Article* as soon as it is available.

You can find more information about *Accepted Manuscripts* in the Information for Authors.

Please note that technical editing may introduce minor changes to the text and/or graphics, which may alter content. The journal's standard Terms & Conditions and the Ethical guidelines still apply. In no event shall the Royal Society of Chemistry be held responsible for any errors or omissions in this *Accepted Manuscript* or any consequences arising from the use of any information it contains.

ROYAL SOCIETY OF CHEMISTRY

www.rsc.org/faraday_d

Modular, Polymer-Directed Nanoparticle Assembly for Fabricating Metamaterials

Gurunatha K. Laxminarayana, Matthew Rozin, Stephanie Smith, and Andrea R. Tao*

NanoEngineering Department, University of California, San Diego

9500 Gilman Drive MC 0448, La Jolla, CA 92093-0448

*E-mail: atao@ucsd.edu

Phone: (858) 822-4237

Fax: (858) 534-9533

ABSTRACT:

We achieve the fabrication of plasmonic meta-atoms by utilizing a novel, modular approach to nanoparticle self-assembly that utilizes polymer templating to control meta-atom size and geometry. Ag nanocubes are deposited and embedded into a polymer thin-film, where polymer embedding depth is used to dictate which nanocube faces are available for further nanocrystal binding. Horizontal and vertical nanocube dimers were successfully fabricated with remarkably high yield using a bifunctional molecular linker to bind a second nanocube. Surface plasmon coupling can be readily tuned by varying the size, shape, and orientation of the second nanoparticle. We show that meta-atoms can be fabricated to exhibit angle- and polarization-dependent optical properties. This scalable technique for meta-atom assembly can be used to fabricate large-area metasurfaces for polarization- and phase-sensitive applications, such as optical sensing.

INTRODUCTION

Optical metamaterials pose major challenges in their fabrication over large areas, which can be prohibitively expensive and time-consuming using conventional nanolithography techniques. In optical metamaterials, metal nanostructures called "meta-atoms" behave as individual optical resonators that must be organized into macroscale arrays to produce the optical response of an effective medium.[1-3] Metamaterial parameters such as effective permittivity and permeability are dictated not only by the size and shape of the meta-atom, but are also strongly dependent on the spacing and arrangement of meta-atoms within the ordered array. This geometric complexity enables tuning of the metamaterial without changing the dielectric environment.[4, 5] On the other hand, the ability to precisely fabricate meta-atom arrays becomes critical for optical performance. Many optical applications such as subwavelength imaging or electromagnetic cloaking also require metamaterials to possess three-dimensional, bulk-like structures.[6-8] As a result, metamaterials are inherently challenging to fabricate due to this multiscale architecture.

Traditional top-down methods for fabricating micrometer-sized arrays of meta-atoms rely on photolithography methods to produce features with a lateral resolution of 20 nm, or direct-write electron-beam lithography methods for sub-10 nm resolution.[9-11] While lithographic techniques are able to define nanostructure location with a high degree of precision, it is difficult to implement fabrication for manufacturing metamaterials or scalable metamaterials processing. In addition, the metal deposition associated with these techniques typically forms nanostructures with rough surfaces or small coalescing grains.[12] As a result, nanolithography produces surface irregularities that present a challenge when fabricating electromagnetic junctions (e.g. the gap in a split-ring resonator, or the spacing between wire-pairs) where metal nanostructures are separated by only a few nanometers. This has led to long-standing difficulties in reproducing

nanojunctions that have been demonstrated to achieve high quality optical resonances. Well-defined, single-crystalline metal nanostructures are highly desirable for improving the quality and consistency of metamaterials performance.

The only nanomaterials that meet these requirements are chemically synthesized nanocrystals (NCs). Metal nanostructures composed of Au and Ag behave like optical antennae by supporting the excitation of localized surface plasmon resonances (LSPRs), where conduction electrons of the metal oscillate in resonance with the incident light wave to produce intense electromagnetic fields localized at the metal surface. Colloidal metal NCs with controlled shapes are ideal building blocks because they can be synthesized in batches using surfactants or polymers that can selectively stabilize low-energy crystal facets[13-16] and are typically single-crystalline. More importantly, these shaped NCs possess LSPRs that can be tuned through chemical synthesis.[17]

Self-assembly provides an ideal approach for metamaterials fabrication that overcomes limitations in scalability, tunability, and design. Self-assembly methods, in contrast to serial methods or lithography, can be carried out on a massively parallel scale using colloidal metal NC building blocks.[18, 19] We and others have successfully demonstrated metal NCs for the assembly of large-area plasmonic materials.[20-22] The NCs have the potential to serve as optical meta-atoms by supporting the excitation of localized surface plasmon resonances (LSPRs) where light impinging on a metal nanostructure couples to the free electrons in the metal.[23, 24] A significant challenge in the self-assembly of colloidal metamaterials is the ability to exhibit precise control over both short-range and long-range NC order to achieve architectures with targeted electromagnetic properties. Several strategies have been developed for achieving the programmable assembly of metal NCs, including the use of DNA linkers,[25, 26] grafted polymers,[5,

[27, 28] or patchy particles.[29-32] However, these methods are typically capable of assembling only small NC clusters. While NCs have been demonstrated to assemble into larger hierarchical structures through the use of capillary or convective assembly,[33, 34] these methods often produce close-packed or diffusion-limited NC clusters that do not provide optimal geometries for optical performance.

To utilize NCs as the building blocks for meta-atoms, the ability to assemble NCs with controlled densities and locations is necessary. For example, periodic arrays of metal NCs deposited at an absorber interface can serve as plasmonic concentrators in a photovoltaic device[35, 36] and two-dimensional arrays of nanoscale split-ring resonators[37] and paired metal stripes[38, 39] have been demonstrated as negative-index metamaterials that have the potential to enable optical elements operating beyond the diffraction limit (e.g. a superlens). We previously demonstrated that polymer-directed assembly could be used to direct the assembly of nanoparticle homojunctions (clusters composed of NC building blocks with the same size and shape)[40] and heterojunctions (clusters composed of different NC building blocks).[41] NCs grafted with different polymer ligands could be assembled into orientations that facilitate maximum electromagnetic field localization. While this polymer-directed assembly method exhibits excellent control over interparticle orientation, it presents a major difficult in controlling NC cluster size and shape. Self-assembly is dictated by NC diffusion through the polymer matrix, and a broad distribution of cluster sizes ranging from populations of single NCs to long NC multimers are produced. We also observed the formation of both linear and branched NC chains, indicating no preferential location for NC attachment during the assembly process. As a result, the optical response of these self-assembled NC clusters is broadband and does not give rise to high quality optical resonances. In order to fabricate meta-atoms based on colloidal NCs, it is

imperative to develop self-assembly methods that enable precise control over NC attachment and NC cluster size.

To address the aforementioned obstacles in self-assembled metamaterials, we move towards a modular, layer-by-layer approach for assembling and positioning colloidal NCs over large areas. (Figure 1) In this approach, NCs will first be assembled into an ordered array at an air-water interface and then deposited onto a polymer support. These NCs serve as templates for sequential NC conjugation to form more complex meta-atoms structures. Both lateral (in-plane) and vertical (out-of-plane) NC arrangement can be precisely controlled to modulate the performance of the resulting colloidal metamaterial. Our assembly experiments target the formation of NC isomers that resemble meta-atoms fabricated using electron-beam and photolithography, such as rods and wires, chains, split-rings, and cross-bars. This stepwise approach to NC assembly bypasses the difficulties associated with diffusion-limited polymer-directed assembly, while at the same time employs techniques that are compatible with scalable nanomanufacturing such as spin-coating and dip-coating.

EXPERIMENTAL METHODS

Chemicals: Silver nitrate ($AgNO_3$), copper chloride ($CuCl_2$), polyvinylpyrrolidone (PVP M.W-55000), citric acid monohydrate ($C_6H_8O_7.H_2O$) were purchased from Sigma Aldrich and used as received. 1,5-Pentane-diol was purchased from Fluka. Polystyrene (M_W=11900) was purchased from Polymer source and poly(ethylene glycol) dithiol **(**PEG dithiol M_W=1000) was purchased from Nanocs chemicals. Analytical grade solvents were used throughout the reaction.

Ag Nanocube Synthesis and purification: Ag nanocubes were synthesized by polyol method reported elsewhere.[40] Briefly, $AgNO_3$ was reduced in a solution of pentanediol, $CuCl_2$ and

polyvinylpyrrolidone. A change in the solution color to an opaque yellow green indicates the formation of nanocubes. PVP plays an active role as a capping agent that controls nanocube nucleation and growth. As synthesized nanocrystals were then characterized by UV-Vis spectroscopy (Agilent Chemstation 8453). Purification of nanocrystals was carried out by diluting the original solution to 50 mL using absolute ethanol and centrifugation using a Thermo Scientific CL2 Centrifuge (2500 rpm for 10 min). The supernatant was isolated and subjected for vacuum filtration with decreasing membrane pore sizes (Millipore Durapore membranes 0.65, 0.40 and 0.22 μm). The final solution was centrifuged at 3400rpm for 60min and re-dispersed with ethanol for the desired concentration.

Nanocomposite Fabrication: Piranha cleaned soda-lime glass substrates (University wafers) were treated with hexamethyldisilazane vapor under vacuum at room temperature for 3 hours to obtain hydrophobic surface. 3.5 wt % of 11k Polystyrene was dissolved in toluene solution and filtered through 0.02 μm pore size filter membrane. A 270 nm thick polystyrene thin-film on the glass substrate was obtained by two-step spinning at 800 rpm for 3 sec and 1700 rpm for 30 sec (WS-400A-6NPP/LITE Laurell Technology Corp). To prepare Ag nanocube films, 2 mL of nanocrystal solution was washed 3 times in ethanol at 3400 rpm for 15min and then residue was re-suspended in 200 μL chloroform ($CHCl_3$). A clean glass petri dish was washed thoroughly and filled with water at convex meniscus. The nanocrystal dispersion was then carefully spread over the air-water interface and the resulting monolayer was left for 15 min to allow for evaporation of organic solvent and monolayer equilibration. Polystyrene coated glass wafers were then dip coated to make nanocube composite film. The area fraction or surface coverage of the nanocube was determined by ImageJ software and by SEM images.

Nanocube embedding: Solvent annealing was carried out by exposing the substrates to $CHCl_3$ vapor in a closed container and samples were taken out and monitored optically and by AFM at different time intervals.Assembly experiments were then carried out.

Surface modification and assembly of Ag nanocubes: For composite films (NC_o), samples were exposed to 2 mL of 12 mM citric acid in ethanol for 15 hours. This was followed by incubation in a 7 mM PEG dithiol solution for 18 hours. The nanocube-polymer substrates were then washed with ethanol to remove excess dithiol from the surface. The removal of excess PVP from Ag nanocube dispersions (NC_1) was carried out by adding 3 mL of 12 mM citric acid in ethanol to 6 mL of the as-synthesized colloidal dispersion, which was stirred vigorously for 3 hours. This dispersion solution was then washed several times by centrifugation and redispersion in neat ethanol. The final precipitate was redispersed in 10 mL of neat ethanol. The nanocube-polymer substrates (NC_o) were then exposed to the washed nanocube dispersions (NC_1) for 15 hours, followed by chemical, optical, and electron microscopy characterization.

Characterization: Raman measurement of the samples was performed on a microRaman spectrometer (Renishaw inVia) in the range of 200 – 1800 cm^{-1}. Samples were illuminated with a 514 nm, 50 mW Argon ion laser. The back-scattered signal was collected on a peltier-cooled (-70 °C) CCD detector with 30 sec acquisition times. Scanning electron microscopy (SEM) characterization was carried out using an ultra-high resolution field emission electron microscope (FEI XL30-SFEG) with an accelerating voltage between 5-15 kV. Optical transmission and extinction spectra were measured using an Agilent Chemstation 8453 in the wavelength range 200-1100nm and optical reflectance spectra were obtained using Perkin – Elmer Lambda 1050 UV-Vis-NIR Spectrometer. Height measurements of Ag nanocubes were carried out upon annealing at different time intervals by atomic force microscope (BRUKER

Innova) operated in the tapping mode. The raw data was processed with Nanoscope IV software by third-order plane fitting and second-order flattening. Measurements were obtained using commercial silicon cantilevers (OLTESPA-R3) with resonance frequency 50-90 kHz and a spring constant near 3.5 N/m.

Finite-Difference Time-Domain (FDTD) simulations: We use two-dimensional FDTD methods to simulate arrays of both horizontally- and vertically-assembled nanocube dimer structures. The horizontal dimer was modeled with NC_o with edge length=100 nm, edge/corner radius of curvature=8 nm, and partially embedded into the polymer matrix with ~40% of the nanocube below the polymer surface. NC_1 (edge length=90 nm, radius of curvature=10 nm) is situated on top of the polymer matrix, its face flush with the polymer surface. The dimer nanojunction is created between the parallel surfaces of the two adjacent nanocube facets, spanning approximately 60 nm high with a gap width of 3 nm. A plane wave is injected normal to the polymer surface, with polarization parallel to the dimer axis. In order to simulate an array of like dimers supported on a continuous substrate, we use periodic (Bloch) boundary conditions in the plane of the supporting substrate, and perfectly-matched layer (PML) boundary conditions normal to the continuous plane. Scattered light is collected behind the light source in the far-field. The vertical dimer utilizes the same nanocube dimensions and boundary conditions as the horizontal dimer, but with an incident source tuned to excite the dimer's coupled dipole-dipole resonance. The plane wave source is injected with angle $\theta=15°$ from normal to the plane of the substrate, with polarization parallel to the plane of incidence. In the vertical dimer geometry, NC_o is 90% embedded in the polymer matrix, and NC_1 is situated directly on top, with a 3 nm gap between the parallel nanocube facets. All FDTD simulations use a 0.5x0.5 nm maximum mesh size, and simulated reflectance spectra span a wavelength range of 200-1000 nm.

RESULTS & DISCUSSION

Modular Nanocrystal Assembly

To build meta-atoms with complex architectures, we use a self-assembly approach where colloidal NCs are assembled onto a polymer or polymer-coated support in a stepwise manner. Dimers, trimers, and other NC isomers were fabricated by engineering NCs to undergo sequential covalent binding events at the polymer interface. (Figure 1) First, colloidal NCs are deposited onto the polymer support. These initial NCs (which we term NC_o) serve as the initial binding platform for all subsequent assembly steps. Second, we carry out solvent or thermal annealing of the polymer support to immobilize and embed the deposited NCs into the polymer. Third, the exposed surfaces of the immobilized NC_o are chemically modified with a covalent molecular linker such as a dithiol. Finally, NC meta-atoms are formed by introducing a second particle (NC_1) that reacts with the molecular linker at the surface of NC_o. This highly modular protocol enables the formation of NC oligomers with controlled geometries and sizes since self-assembly is dictated by the accessibility of the molecular linker. In principle, these assembly steps can be cycled to produce hierarchical or dendritic NC motifs, or can be applied for the fabrication of hetero-NC oligomers composed of mismatched NCs. In this manner, the combinatorial formation of NC meta-atoms can be highly controlled by using different types of plasmonic nanoparticle for NC_o and NC_1. Figure 1B shows an example of our results when Ag nanocubes (edge length = 70 nm), Au nanospheres (diameter=25nm), Ag nanospheres (diameter = 44 nm), Ag nanoprisms, or Ag nanorods are employed as NC_1.

To demonstrate the feasibility of generating meta-atoms arrays using this modular approach, we focused on the formation of meta-atoms where Ag nanocubes are used as both NC_o

and NC_1. Colloidal Ag nanocubes were synthesized via a polyol method,[40, 42] where $AgNO_3$ is reduced in a solution of pentanediol, $CuCl_2$, and polyvinylpyrrolidone (PVP) (M_w=55,000). PVP serves as a selective capping agent that controls nanocube nucleation and growth and also serves to passivate the surface of the Ag NCs during the assembly process. The as-made Ag nanocube dispersion was concentrated by centrifuging the dispersion (3400 rpm for 60 min.) and reconstituting the precipitate in chloroform. This dispersion was then deposited drop-wise onto the air-water interface of a glass petri dish filled with deionized water (18 MΩ) and allowed to equilibrate for 15 min. NC arrays were generated by dip-coating polystyrene (PS)-coated glass slides through the air-water interface. These nanocubes serve as NC_o during the assembly process. Large interparticle spacings (>100 nm) within the NC array are preserved by the presence of long PVP grafts that remain chemisorbed to the Ag surface of the colloidal nanocubes.

The deposited arrays were then subjected to solvent annealing with chloroform vapor to embed the nanocubes in the underlying polystyrene thin-film. The polymer embedding depth of NC_o constrains meta-atom assembly by exposing or protecting the metal surface of NC_o from chemical modification with a molecular linker. Embedding depth can be precisely controlled by solvent annealing time. Analogous to a two-dimensional melt processing step,[43] solvent absorption leads to a free volume increase in the polymer and reduced adhesion between polymer chains. An increase in the mobility of polymer chains allows vertical diffusion of the NC into the polymer film. Figure 2 shows scanning electron microscope (SEM) images of 100 nm Ag nanocubes that have been deposited onto a PS thin-film that is 270 nm thick, and then solvent annealed for 33, 53, and 63 minutes. The extinction spectra (Figure S1) and atomic force microscope (AFM) topology maps of these arrays (Figure S2) clearly show the vertical mobility

of Ag NCs. This is further confirmed by a continuous red shift of the dipolar and quadrupolar LSPRs of the Ag NCs with increasing solvent annealing time, which is attributed to an increase in the refractive index of the NC environment as it diffuses into the PS film (Figure S1). The corresponding AFM height measurements of the PS-embedded nanocubes show that embedding depth can be controlled down to 10 nm increments.

Surface Modification and Self-Assembly

The partially embedded Ag NCs were then surface functionalized with a bifunctional PEG dithiol linker in order to facilitate binding of a second NC. To carry out surface functionalization, removing chemisorbed PVP from the Ag surface of NC_o was necessary. This was carried out by treating the exposed surfaces of NC_o with citric acid (see experimental section for the detailed procedure), which has been shown to displace PVP chains by mild oxidative etching.[44] Raman spectroscopy of the treated NC_o nanocubes (Figure S3) confirm partial removal of PVP and the presence of citric acid on the nanocube surface. Next, the treated NC_o surfaces were incubated with a solution of PEG dithiol, which serves as the molecular linker. Raman spectroscopy shows complete displacement of both PVP and citrate by the dithiol. Raman spectra also indicate the presence of the terminal –SH group (Figure S3), which is available for binding upon exposure to NC_1 nanocubes.

The dithiol-modified nanocubes were then exposed to dispersions of as-made Ag nanocubes with edge lengths of 70 nm, which serve as NC_1. Figure 3 shows the results of nanocube assembly for three different NC_o embedding depths: 15 nm, 42 nm and 61 nm. Inspection of SEM images over an area of 25 μm^2 revealed that with an embedding depth of 15 nm (Figure 3A), the resulting nanocube assemblies consist of only 16% dimers (Figure 3D).

Additionally, 39% of meta-atoms are trimers and 36% are larger multimers with NC_1 binding horizontally on NC_o sidewalls as well as vertically on the top NC_o surface. With an increased embedding depth (Figures 3B, 3C), we observe a reduction in the population of trimers and multimers along a large increase in the population of nanocube dimers. This is attributed to the decreased surface area available for NC_1 binding. For an embedding depth of 60 nm (Figure 3C) where nearly all of the NC_o side surfaces are protected by PS, a dimer population of 89% was achieved.

Optical extinction spectra were collected for the meta-atom assemblies at normal incidence and reveal the appearance of new LSPR bands that arise from surface plasmon coupling. This LSPR band appears at wavelengths of between 650-700 nm for the assembled structures. In addition, we observe a blue-shift of the dipolar and quadrupolar LSPR bands attributed to isolated Ag NC_o nanocubes (black curves). This LSPR shift is correlated to both the embedding depth of NC_o and to plasmon coupling. For an embedding depth of 60 nm, the LSPR peak attributed to a coupled mode at 651 nm (Figure 3I) is very weak despite the dominant dimer population. This is attributed to the dimer geometry, which is oriented orthogonal to the polymer-air interface of the substrate. This suggests the meta-atoms assemblies are highly polarized, depending on assembly orientation and geometry.

Optical Characterization

Using FDTD methods, we modeled the optical response from horizontal (dimer axis oriented parallel to the substrate) and vertical (dimer axis oriented orthogonal to the substrate) dimers. Figure 4 shows the simulated optical reflectance spectra and representative resonant electric field distributions for horizontal and vertical Ag nanocube dimers where NC_o=100 nm and NC_1=90

nm. We find that spectral features below 500 nm are correlated with LSPR modes where the electric fields are localized on individual nanocubes, whereas features above 500 nm possess electric fields that are highly localized in the interstitial gap between the nanocubes. These gap modes are the result of strong electromagnetic coupling. In the reflectance spectra for both dimer orientations, the most intense and lowest energy reflectance peak correlates with excitation of the fundamental, or lowest-order dipolar gap mode. For the horizontal dimer, this fundamental gap mode is excited at λ=733 nm and the optical field is highly concentrated between the corner of one cube and the face of the other cube, as shown in the field distribution map in Figure 4B. For the vertical dimer, the fundamental gap mode is excited at λ=735 and the field is highly symmetric within the interstitial gap (Figure 4E). Reflectance peaks at shorter wavelengths resulting from higher-order gap modes, and in some cases, overlap significantly with other LSPR modes. A quadrupolar gap mode is observed for the horizontal dimer at λ=500 (Figure 4C) and for the vertical dimer at λ=460 nm (Figure 4E). In the case of the vertical dimer, interference between multiple reflections within the nanojunction results in peak splitting and broadening of the reflectance peak associated with the fundamental mode.

To confirm these simulation results, we carried out angle- and polarization-dependent reflectance measurements from horizontal dimers with NC_o= 100 nm Ag nanocubes at an embedding depth of 42 nm, and NC_1=90 nm Ag nanocubes, as shown in Figure 5. Reflectance spectra were recorded at two different incident angles of θ = 4° (black) and θ = 33° (red) with both s- and p-polarized light. At incident angle θ = 4°, the LSPR modes resulting from coupling appears as an intense reflectance band at λ=732 nm (from the dipolar mode) and at λ=504 nm (from the quadrupolar mode) irrespective of s- or p- (Figure 5C, D, black curves). This is because the field component of both s- and p- polarized light match with the geometric axis of

the horizontal dimers, exciting the fundamental gap mode of the nanocube pair. At incident angle θ = 33°, illumination with p-polarized light results in the disappearance of this coupled LSPR mode, since the direction of polarization is no longer aligned with the nanocube dimer axes. (Figure 5C, red curve) For the same angle of illumination with s-polarized light, we observe a large increase in overall reflectance, since the polymer thin-film behaves as a standard dielectric interface. The dipolar coupled LSPR mode is still not excited due to the mismatch between polarization and dimer orientation (Figure 5D, red curve).

Figure 6 shows the angle- and polarization-dependent reflectance spectra for vertical nanocube dimers with NC_o=100 nm Ag nanocubes at an embedding depth of 60 nm, with NC_1=90 nm. At near-incidence illumination angles of θ = 4°, both s- and p-polarization show limited evidence of plasmon coupling and only the LSPR modes associated with individual nanocubes are excited. For these dimers, illumination with p-polarized light at an incident angle of θ = 33° is the only configuration that can give rise to the coupled dipole-dipole LSPR mode. This is observed in Figure 6C (red curve) at λ=735 nm, where the intensity of the nanocube gap mode dominates almost the entire reflectance spectrum. For s-polarized light and an incident angle of θ = 33°, the reflectance spectrum gives rise to a broadband feature in the longer wavelengths, similar to what is observed for horizontal dimers.

Finally, we demonstrate that LSPR wavelength and strength of the coupled mode can be tuned by varying NC_1 size. Figure 7 shows the optical extinction spectra for horizontal nanocube dimers composed of NC_o=100 nm Ag nanocubes at an embedding depth of 42 nm, and NC_1=64 nm, 70 nm, and 90 nm. For NC_1=64 nm, the coupled LSPR mode appears at λ=677 nm. As NC_1 size is increased, the wavelength of this fundamental mode red-shifts and increases in extinction intensity. With the attachment of 64 nm cubes (Figure 7A), the LPSR mode was red shifted to

λ=700 for NC_1=70 nm cubes (Figure 7B) and to λ=726 nm for NC_1=90 nm cubes (Figure 7C). The intensity of this coupled mode is correlated with the strength of light confinement in the dimer gap. Figure 7D shows simulation results for horizontal dimers with NC_o=100 nm Ag nanocubes and NC_1=60-110 nm Ag nanocubes separated by a gap of 3 nm. The wavelength position of the lowest-order fundamental gap mode is plotted with respect to NC_1 size. The redshift in reflectance peak wavelength closely matches a linear regression, which is consistent with the electromagnetic response for dipole-dipole coupling. We also find that the strongest optical coupling occurs for nanocube pairs where size mismatch is minimal.

CONCLUSIONS

We demonstrate that meta-atoms can be fabricated using a modular, polymer-templated approach that can be readily scaled over large surface areas. In particular, nanocube dimer arrays can be fabricated over a few square centimeters with yields of almost 90%. This is a promising proof-of-concept demonstration that self-assembly is a viable technique for bottom-up, polymer-based metamaterials. Furthermore, our method has the potential to achieve the assembly of more complex meta-atoms structures by assembling NCs in a combinatorial fashion, or by carrying out multiple layer-by-layer assembly.

ASSOCIATED CONTENT

Supporting Information: Extinction spectra of Ag nanocubes with various embedding depths and corresponding AFM analysis; Raman spectra of surface-functionalized Ag nanocubes.

ACKNOWLEDGEMENTS

This work is funded by the Office of Naval Research (Award No.N000141210574) and a grant from National Science Foundation (CMMI, Award No. 1200850).

FIGURES

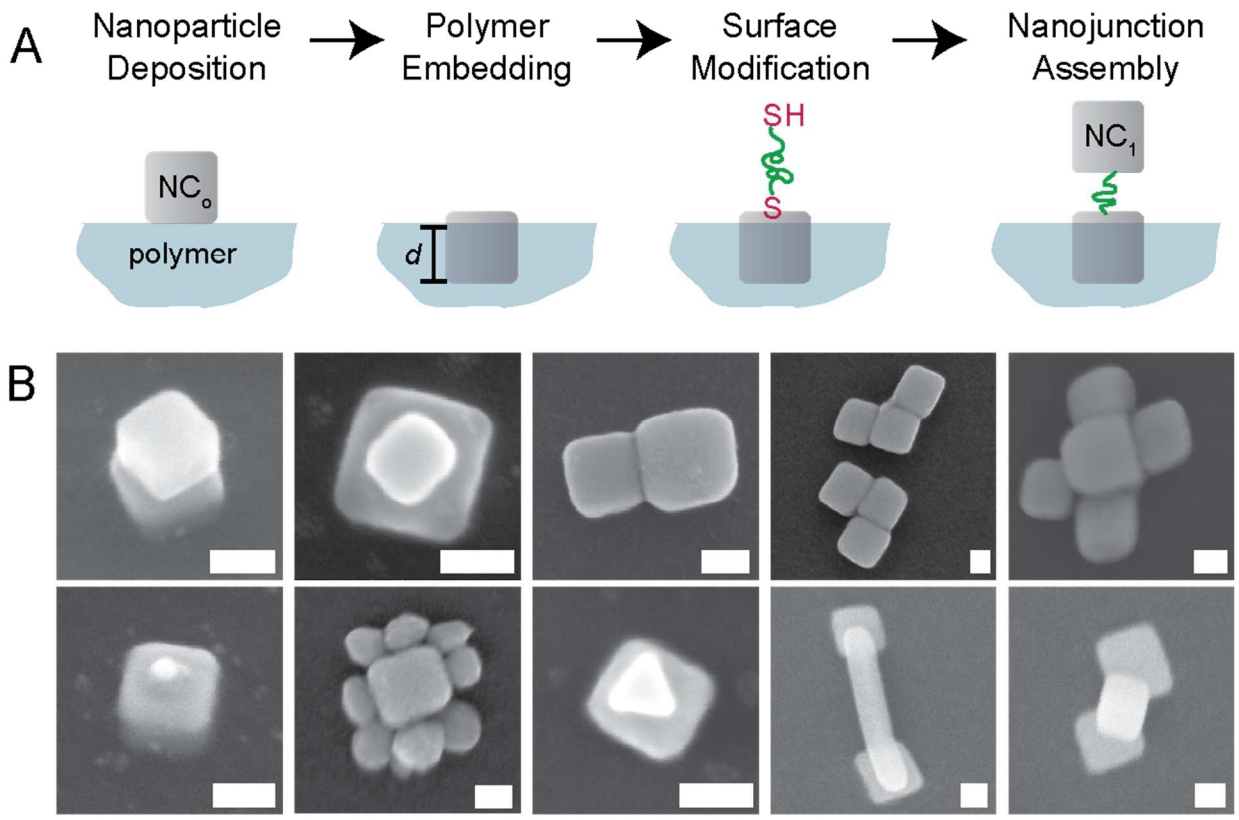

Figure 1. (A) Schematic of stepwise, modular NC assembly using Ag nanocubes to form dimer and cross-like meta-atoms. (B) Meta-atom assemblies for various combinations of NC_o and NC_1. Scale bar = 50 nm.

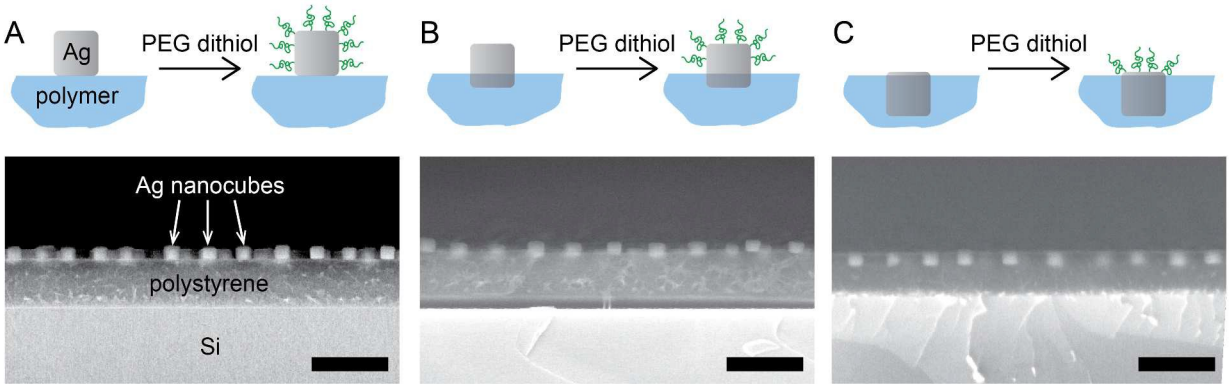

Figure 2. Schematic of nanocube embedding into a polymer thin-film and surface modification with a bifunctional polymer graft. Tilted SEM pictures of Nanocube on PS thin-film embedded at 15 nm, 42 nm and 61 nm. Scale bar = 500 nm.

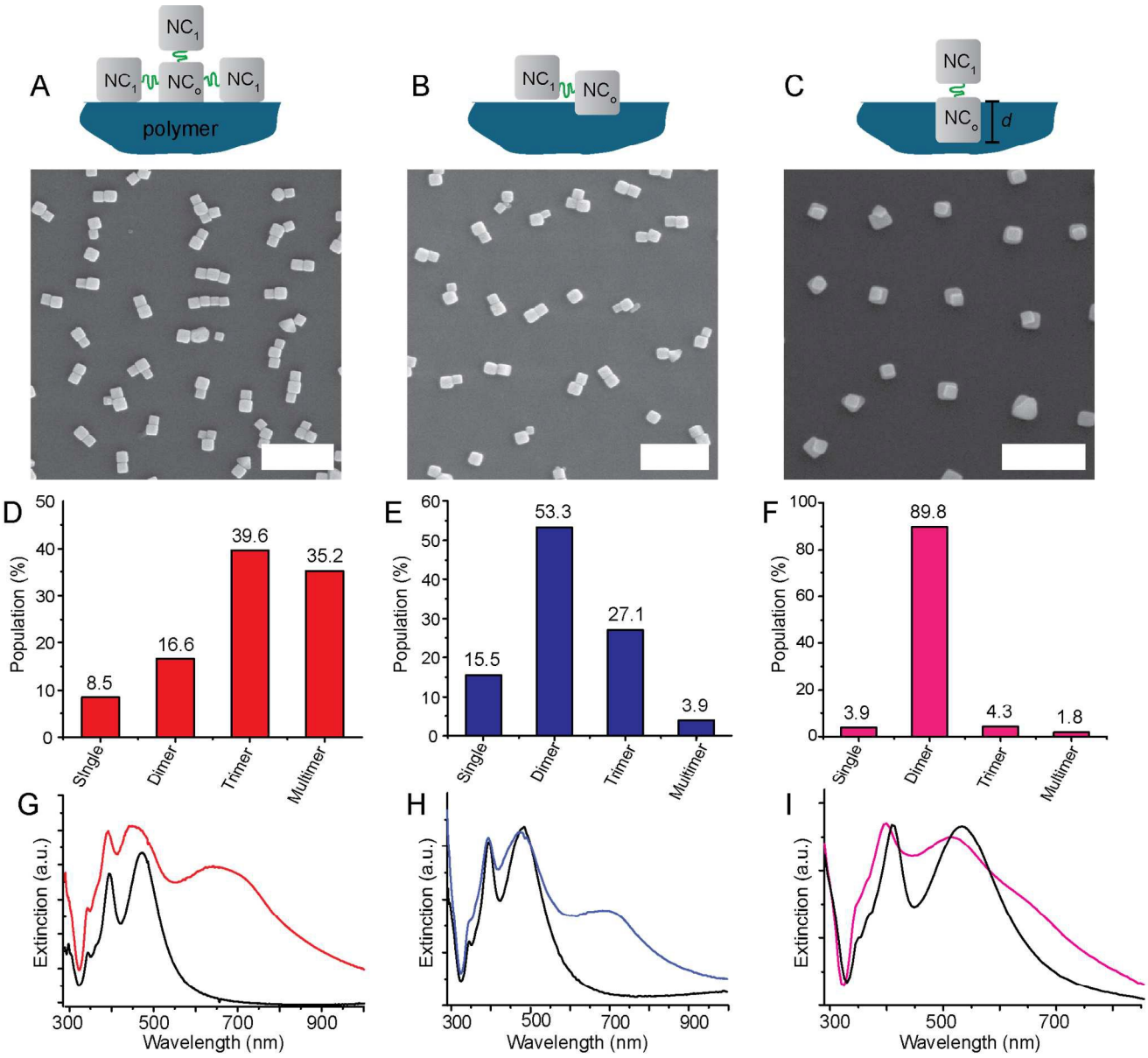

Figure 3. (A-C) Schematic and SEM image of nanocube assembly observed at embedding depth of 15 nm, 42 nm and 61 nm of NC_o. Scale bar = 500 nm. (D-F) Corresponding statistical analysis showing the population distributions of monomers, dimers, trimers, and multimers in each assembly. (G-I) Corresponding optical extinction spectra taken an incident illumination with a broadband white light source. The extinction spectrum of as-deposited NC_o nanocubes prior to modular assembly is shown for reference (black lines).

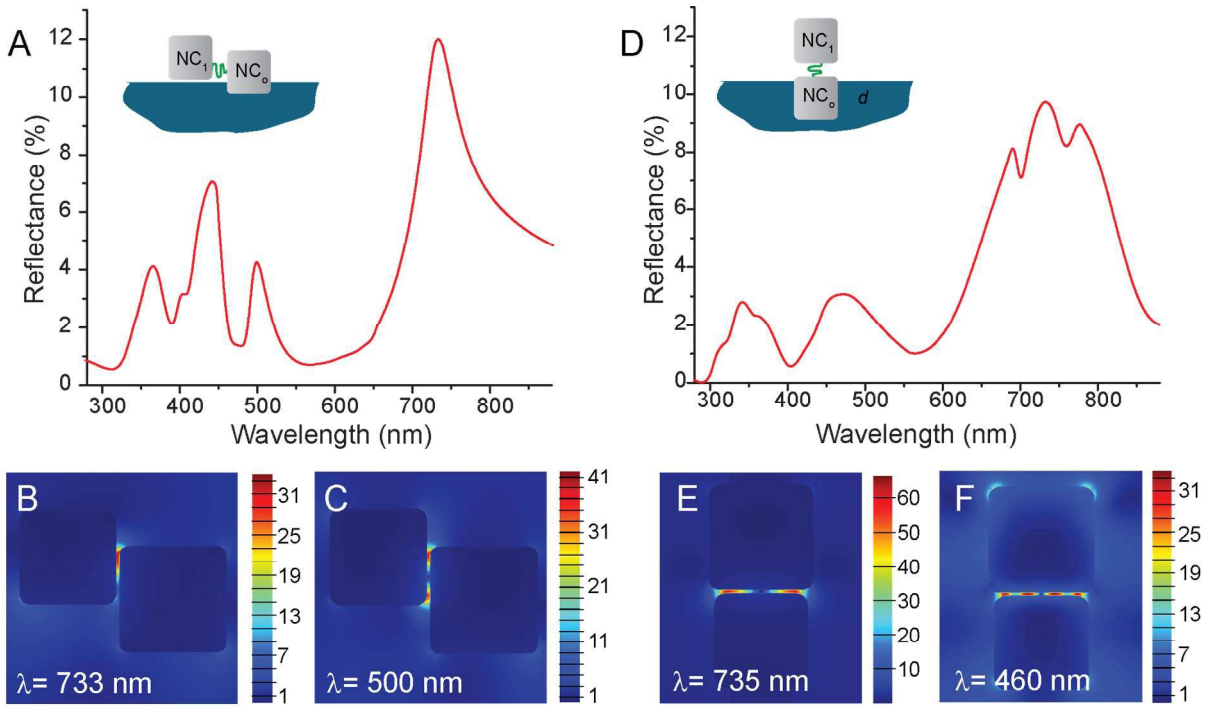

Figure 4. Simulated optical reflectance and near-field distributions for (A-C) horizontally-assembled and (D-F) vertically-assembled Ag nanocube dimer arrays. In all simulations, NC_o=100 nm Ag nanocube and NC_1=90 nm Ag nanocube. (B, C) Horizontal dimer cross-section showing the electric-field distributions for resonances at (B) λ=733 nm and (C) λ=500 nm. (E,F) Vertical dimer cross-section showing the electric-field distributions for resonances at (E) λ=735 and (F) λ=460 nm, respectively.

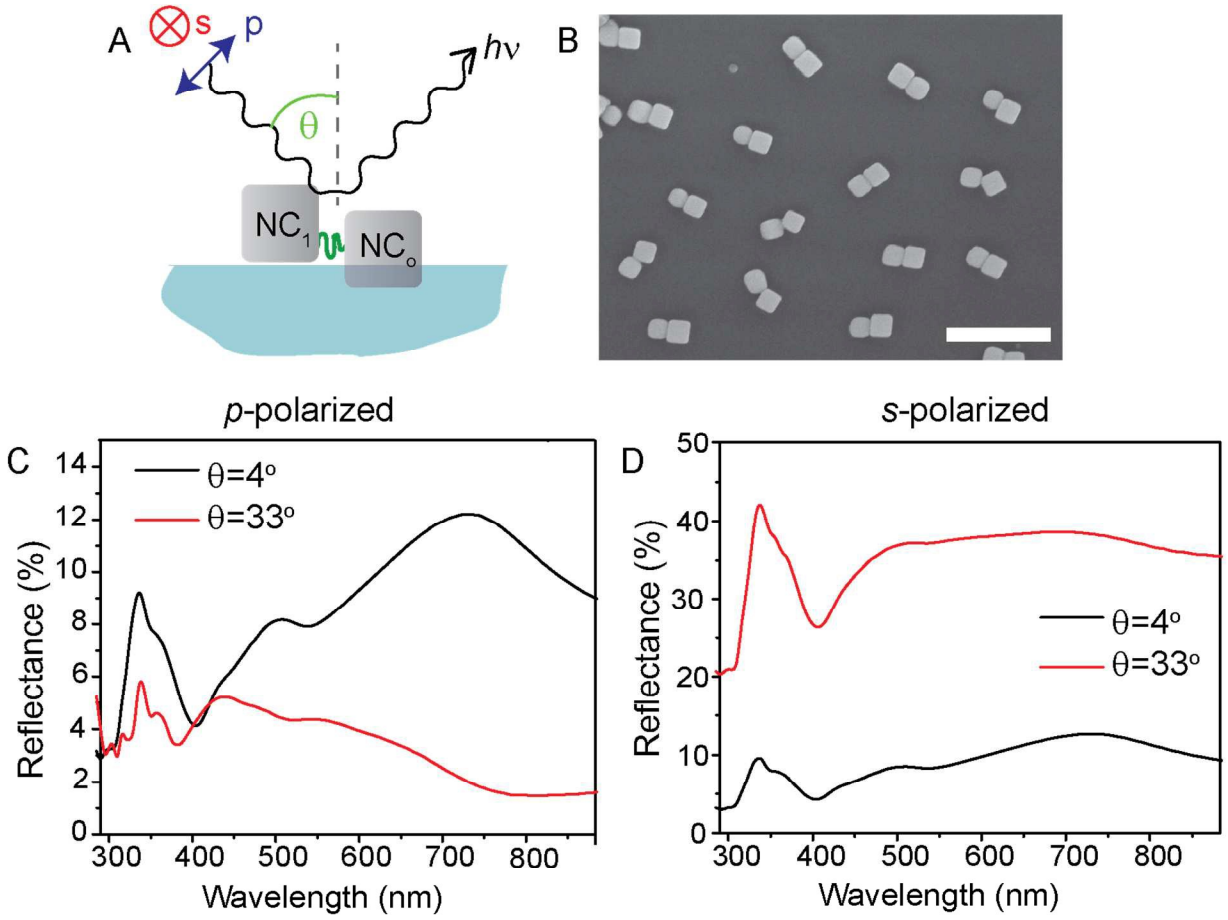

Figure 5. (A) Schematic of optical reflectance measurements showing directions of s- and p-polarized light for a horizontal nanocube dimer as shown in the SEM image in (B). (C-D) Corresponding optical reflectance spectra taken at an incident angles of θ = 4° (black) and θ = 33° (red) with p- and s-polarized light, respectively.

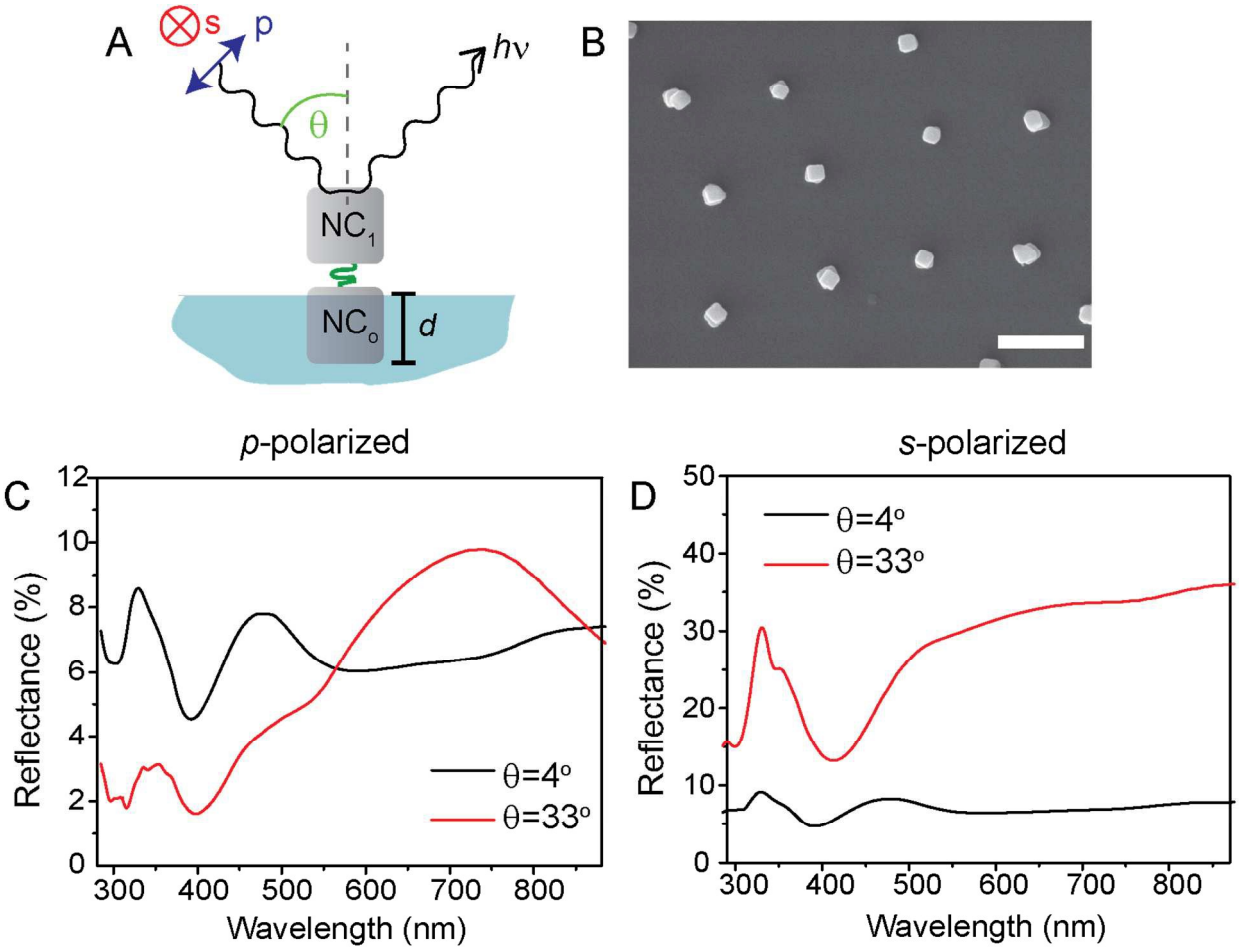

Figure 6. (A) Schematic of optical reflectance measurements showing directions of s- and p-polarized light for a vertical nanocube dimer as shown in the SEM image in (B). (C-D) Corresponding optical reflectance spectra taken at an incident angles of θ = 4° (black) and θ = 33° (red) with p- and s-polarized light, respectively.

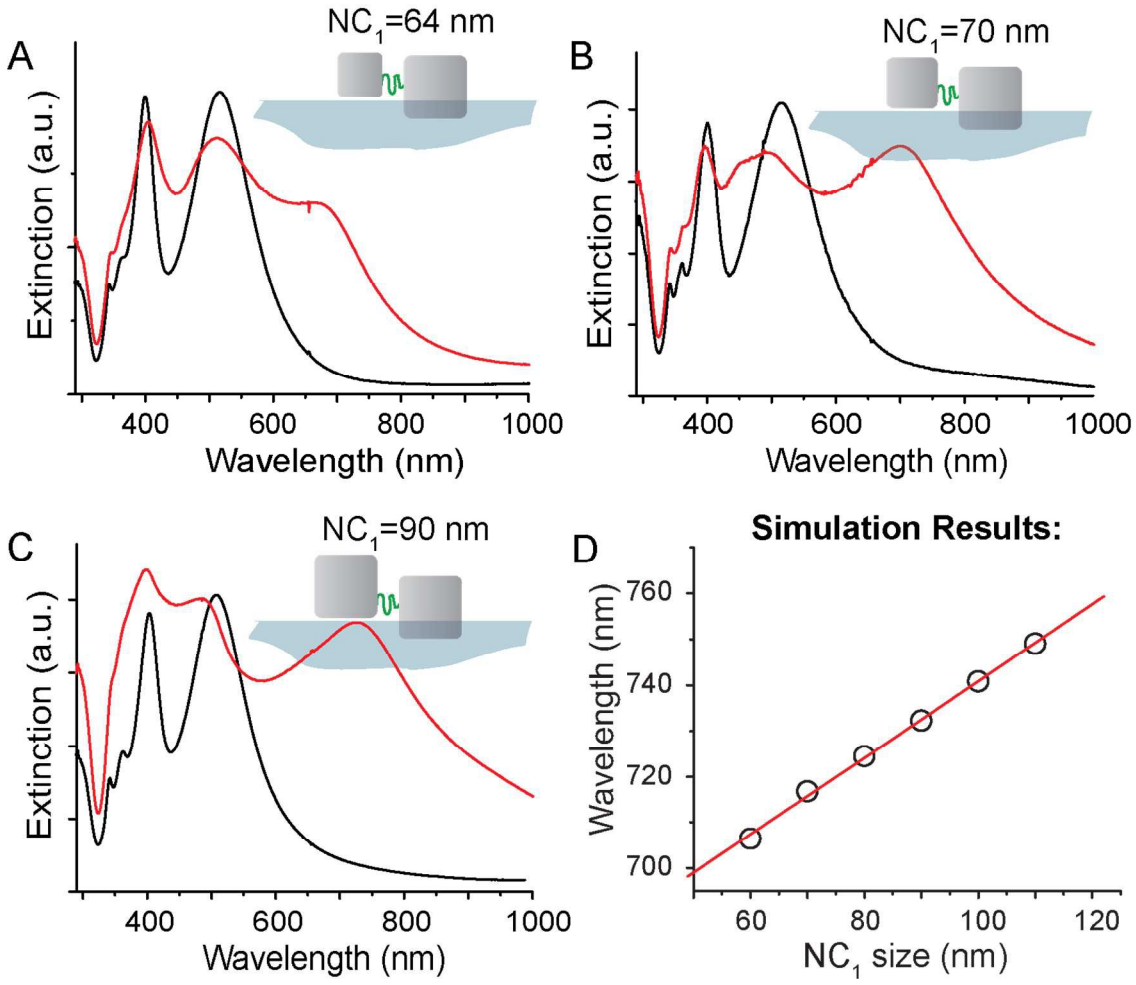

Figure 7. (A-C) Extinction spectra of horizontal dimers with varying NC_1 nanocube sizes of (A) 64 nm, (B) 70 nm, and (C) 90 nm. The extinction spectrum of as-deposited NC_o nanocubes prior to modular assembly is shown in black for each sample. (D) Plot of the shift in dipole-dipole coupling mode with respect to NC_1 size, obtained from simulated reflectance spectra.

REFERENCES:

1. A. Pors, O. Albrektsen, I. P. Radko and S. I. Bozhevolnyi, *Sci. Rep.*, 2013, **3**.
2. S. Sun, K.-Y. Yang, C.-M. Wang, T.-K. Juan, W. T. Chen, C. Y. Liao, Q. He, S. Xiao, W.-T. Kung, G.-Y. Guo, L. Zhou and D. P. Tsai, *Nano Letters*, 2012, **12**, 6223-6229.
3. X. Ni, N. K. Emani, A. V. Kildishev, A. Boltasseva and V. M. Shalaev, *Science*, 2012, **335**, 427-427.
4. B. Kanté, A. de Lustrac and J. M. Lourtioz, *Physical Review B*, 2009, **80**, 035108.
5. G. Dolling, C. Enkrich, M. Wegener, J. F. Zhou, C. M. Soukoulis and S. Linden, *Opt. Lett.*, 2005, **30**, 3198-3200.
6. N. Liu, H. Guo, L. Fu, S. Kaiser, H. Schweizer and H. Giessen, *Nature materials*, 2008, **7**, 31-37.
7. J. Valentine, S. Zhang, T. Zentgraf, E. Ulin-Avila, D. A. Genov, G. Bartal and X. Zhang, *nature*, 2008, **455**, 376-379.
8. C. M. Soukoulis and M. Wegener, *Nature Photonics*, 2011, **5**, 523-530.
9. C. L. Holloway, D. C. Love, E. F. Kuester, A. Salandrino and N. Engheta, *Microwaves, Antennas & Propagation, IET*, 2008, **2**, 120-129.
10. A. L. Koh, A. I. Fernández-Domínguez, D. W. McComb, S. A. Maier and J. K. W. Yang, *Nano Letters*, 2011, **11**, 1323-1330.
11. M. Bresin, N. Nehru and J. T. Hastings, 2013.
12. Y. Xia, J. A. Rogers, K. E. Paul and G. M. Whitesides, *Chemical Reviews*, 1999, **99**, 1823-1848.
13. R. Jin, Y. Cao, C. A. Mirkin, K. L. Kelly, G. C. Schatz and J. G. Zheng, *Science*, 2001, **294**, 1901-1903.

14. B. Nikoobakht and M. A. El-Sayed, *Chemistry of Materials*, 2003, **15**, 1957-1962.

15. A. Tao, P. Sinsermsuksakul and P. Yang, *Angewandte Chemie International Edition*, 2006, **45**, 4597-4601.

16. Y. Xia, Y. Xiong, B. Lim and S. E. Skrabalak, *Angewandte Chemie International Edition*, 2009, **48**, 60-103.

17. J. J. Mock, M. Barbic, D. R. Smith, D. A. Schultz and S. Schultz, *The Journal of Chemical Physics*, 2002, **116**, 6755-6759.

18. Z. Nie, A. Petukhova and E. Kumacheva, *Nat Nano*, 2009, **5**, 15-25.

19. G. M. Whitesides and B. Grzybowski, *Science*, 2002, **295**, 2418-2421.

20. C. Ciracì, R. T. Hill, J. J. Mock, Y. Urzhumov, A. I. Fernández-Domínguez, S. A. Maier, J. B. Pendry, A. Chilkoti and D. R. Smith, *Science*, 2012, **337**, 1072-1074.

21. B. Gao, M. J. Rozin and A. R. Tao, *Nanoscale*, 2013, **5**, 5677-5691.

22. M. Rycenga, C. M. Cobley, J. Zeng, W. Li, C. H. Moran, Q. Zhang, D. Qin and Y. Xia, *Chemical Reviews*, 2011, **111**, 3669-3712.

23. N. I. Landy, S. Sajuyigbe, J. J. Mock, D. R. Smith and W. J. Padilla, *Physical Review Letters*, 2008, **100**, 207402.

24. A. V. Kildishev, A. Boltasseva and V. M. Shalaev, *Science*, 2013, **339**.

25. D. Nykypanchuk, M. M. Maye, D. van der Lelie and O. Gang, *Nature*, 2008, **451**, 549-552.

26. S. Y. Park, A. K. R. Lytton-Jean, B. Lee, S. Weigand, G. C. Schatz and C. A. Mirkin, *Nature*, 2008, **451**, 553-556.

27. P. Akcora, H. Liu, S. K. Kumar, J. Moll, Y. Li, B. C. Benicewicz, L. S. Schadler, D. Acehan, A. Z. Panagiotopoulos, V. Pryamitsyn, V. Ganesan, J. Ilavsky, P. Thiyagarajan, R. H. Colby and J. F. Douglas, *Nat Mater*, 2009, **8**, 354-359.

28. R. Shenhar, T. B. Norsten and V. M. Rotello, *Advanced Materials*, 2005, **17**, 657-669.

29. K. K. Caswell, J. N. Wilson, U. H. F. Bunz and C. J. Murphy, *Journal of the American Chemical Society*, 2003, **125**, 13914-13915.

30. G. A. DeVries, M. Brunnbauer, Y. Hu, A. M. Jackson, B. Long, B. T. Neltner, O. Uzun, B. H. Wunsch and F. Stellacci, *Science*, 2007, **315**, 358-361.

31. C.-L. Chen, P. Zhang and N. L. Rosi, *Journal of the American Chemical Society*, 2008, **130**, 13555-13557.

32. Z. Nie, D. Fava, E. Kumacheva, S. Zou, G. C. Walker and M. Rubinstein, *Nat Mater*, 2007, **6**, 609-614.

33. T. Ming, X. Kou, H. Chen, T. Wang, H.-L. Tam, K.-W. Cheah, J.-Y. Chen and J. Wang, *Angewandte Chemie International Edition*, 2008, **47**, 9685-9690.

34. F. Li, W. C. Yoo, M. B. Beernink and A. Stein, *Journal of the American Chemical Society*, 2009, **131**, 18548-18555.

35. V. E. Ferry, L. A. Sweatlock, D. Pacifici and H. A. Atwater, *Nano Letters*, 2008, **8**, 4391-4397.

36. R. A. Pala, J. White, E. Barnard, J. Liu and M. L. Brongersma, *Advanced Materials*, 2009, **21**, 3504-3509.

37. D. R. Smith, W. J. Padilla, D. C. Vier, S. C. Nemat-Nasser and S. Schultz, *Physical Review Letters*, 2000, **84**, 4184.

38. V. M. Shalaev, W. Cai, U. K. Chettiar, H.-K. Yuan, A. K. Sarychev, V. P. Drachev and A. V. Kildishev, *Opt. Lett.*, 2005, **30**, 3356-3358.

39. V. M. Shalaev, *Nat Photon*, 2007, **1**, 41-48.

40. B. Gao, G. Arya and A. R. Tao, *Nat Nano*, 2012, **7**, 433-437.

41. B. Gao, Y. Alvi, V. Li and A. R. Tao, *CrystEngComm*, 2014, **16**, 9434-9440.

42. Y. Sun and Y. Xia, *Science*, 2002, **298**, 2176-2179.

43. M. E. Mackay, A. Tuteja, P. M. Duxbury, C. J. Hawker, B. Van Horn, Z. Guan, G. Chen and R. S. Krishnan, *Science*, 2006, **311**, 1740-1743.

44. Y. Xiong, *Chemical Communications*, 2011, **47**, 1580-1582.